Description of hard-sphere crystals and crystal-fluid interfaces: A comparison between density functional approaches and a phase-field crystal model

M. Oettel,[1,2] S. Dorosz,[3] M. Berghoff,[4] B. Nestler,[4] and T. Schilling[3]

[1]*Johannes Gutenberg-Universität Mainz, Institut für Physik, WA 331, D-55099 Mainz, Germany*

[2]*Institut für Theoretische Physik II, Heinrich-Heine-Universität Düsseldorf, D-40225 Düsseldorf, Germany*

[3]*Université du Luxembourg, Theory of Soft Condensed Matter, L-1511 Luxembourg, Luxembourg*

[4]*Institute of Applied Materials, Karlsruhe Institute of Technology, D-76131 Karlsruhe, Germany*

(Received 25 June 2012; published 22 August 2012)

In materials science the phase-field crystal approach has become popular to model crystallization processes. Phase-field crystal models are in essence Landau-Ginzburg-type models, which should be derivable from the underlying microscopic description of the system in question. We present a study on classical density functional theory in three stages of approximation leading to a specific phase-field crystal model, and we discuss the limits of applicability of the models that result from these approximations. As a test system we have chosen the three-dimensional suspension of monodisperse hard spheres. The levels of density functional theory that we discuss are fundamental measure theory, a second-order Taylor expansion thereof, and a minimal phase-field crystal model. We have computed coexistence densities, vacancy concentrations in the crystalline phase, interfacial tensions, and interfacial order parameter profiles, and we compare these quantities to simulation results. We also suggest a procedure to fit the free parameters of the phase-field crystal model. Thereby it turns out that the order parameter of the phase-field crystal model is more consistent with a smeared density field (shifted and rescaled) than with the shifted and rescaled density itself. In brief, we conclude that fundamental measure theory is very accurate and can serve as a benchmark for the other theories. Taylor expansion strongly affects free energies, surface tensions, and vacancy concentrations. Furthermore it is phenomenologically misleading to interpret the phase-field crystal model as stemming directly from Taylor-expanded density functional theory.

DOI: 10.1103/PhysRevE.86.021404 PACS number(s): 82.70.Dd, 61.50.Ah, 71.15.Mb

I. INTRODUCTION

In materialsscience, the modeling of dynamic processes involving the growth of solid phases in melts or in the environment of another solid phase has been advanced using phase-field models in the past years [1,2]. Here the phase field φ is associated with an order parameter field that distinguishes between a solid and a liquid phase, and it is usually coupled with a density or concentration field ϱ for that phase. The dynamics of ϱ is conserved, following the equation

$$\frac{\partial \varrho}{\partial t} = \nabla \cdot (\Gamma_\varrho \mathbf{j}_\varrho), \tag{1}$$

$$\mathbf{j}_\varrho(\mathbf{r},t) = \nabla \frac{\delta \mathcal{F}[\varrho,\varphi]}{\delta \varrho(\mathbf{r},t)}. \tag{2}$$

Here the density current $\mathbf{j}_\varrho$ is the gradient of a chemical potential function which is assumed to be derivable from a free energy functional $\mathcal{F}$. Γ_ϱ is a mobility. In contrast to this, there is no conservation law for the order parameter, and thus one can generically assume a nonconserved dynamic evolution of φ of the form

$$\frac{\partial \varphi}{\partial t} = \tilde{\Gamma}_\varphi \frac{\delta \mathcal{F}[\varrho,\varphi]}{\delta \varphi(\mathbf{r})}. \tag{3}$$

In order to briefly explain the approach, we consider a one-component system able to form one fluid and one solid phase. The simplest free energy functional which gives us phase coexistence associated with smoothly varying profiles for ϱ and φ across the phase boundary follows from a gradient expansion in the specific truncation

$$\mathcal{F}[\varrho,\varphi] = \frac{F_0}{k_B T} \int d^3r [c_2(\nabla\varphi)^2 + f(\varrho,\varphi)]. \tag{4}$$

Here it is assumed that any inhomogeneity costs free energy through the gradient term in the order parameter field. Since there is no corresponding gradient term in the density, the free energy penalty corresponding to a change in the density field must be small, and this appears to be possible only if ϱ is suitably coarse-grained from the microscopic density field. Consequently the variations in the microscopic density field relevant for the free energy must be contained in the phase field φ, which in turn should be derivable from the microscopic density through another coarse-graining procedure. We will return to that point below. The potential function $f(\varrho,\varphi)$ contains a double-well-type expression with minima at $\varphi = -1$ (fluid) and $\varphi = 1$ (solid), modified such that minimization with respect to ϱ gives the input fluid and crystal coexistence densities $\varrho_{\rm fl}(T)$ and $\varrho_{\rm cr}(T)$, which in general depend on the temperature T. A possible form is [2]

$$f(\varrho,\varphi) = g_1(\varphi) + \tfrac{1}{2}[1+g_2(\varphi)] f_{\rm cr}(\varrho) + \tfrac{1}{2}[1-g_2(\varphi)] f_{\rm fl}(\varrho), \tag{5}$$

with
$$g_1(\varphi) = (\varphi+1)^2(\varphi-1)^2, \tag{6}$$

and
$$g_2(\varphi=\pm1) = \pm1, \quad g_2'(\varphi=\pm1) = 0. \tag{7}$$

Thus, the phase-field approach is nothing but a slightly rewritten Landau-Ginzburg model for the fluid-solid phase transition. The formulation accommodates an empirical free energy density for the fluid phase $[f_{\rm fl}(\varrho)]$ and the crystal phase $[f_{\rm cr}(\varrho)]$, yielding the required input coexistence densities. In the form of Eq. (4), the free energy contains the parameters F_0 related to is the free energy scale in units of the thermal energy $k_B T$ (should be adjusted to the bulk free energy difference

of solid and liquid) and the constant c_2, which can be fixed through the value of the liquid-solid surface tension.

In such a way, nucleation and growth in simple systems can be addressed without resolving the details of the free energy for inhomogeneous systems. For the widely used hard-sphere reference system (which will be examined more in detail in this work), this has been done in, e.g., Ref. [3].

Such a minimal Landau-Ginzburg description can be extended to more complex systems. For each new material component of the system, one needs to introduce a corresponding density field, and new phase fields for the fluid and solid phases, even when the solid phases differ just by their crystalline orientation. Thus the number of free energy and surface tension parameters quickly grows when the complexity of the system is increased. Even for the one-component system, empirical information on the anisotropy of the surface tension for different crystal faces in equilibrium with the fluid needs to be taken into account to set the parameters. Hence an important question is whether the phase field itself can be consistently treated in terms of the density field which stems from a microscopic foundation.

In this paper we investigate three formulations (or approximations) to classical density functional theory which deal with the microscopic particle density field and thus, in principle, constitute the underlying theoretical framework from which a consistent phase-field crystal description should arise. In our explicit calculations, we examine the coexistence properties, surface tensions, and interface density modes in the hard-sphere system. Understanding surface tensions for different interface orientations and the associated surface structure are important prerequisites for further studies. There are three main reasons to choose the hard-sphere system for method comparison: (1) availability of very precise density functionals (fundamental measure theory, our first formulation); (2) empirical evidence that the crystal-liquid surface tensions of fcc(hcp)-forming metals are largely of entropic origin, and thus the packing of impenetrable cores plays an important role for the surface structure of these metals [4]; and (3) the athermal nature of the hard-sphere system, which reduces the parameters for describing the coexistence to just the pair of coexistence densities for the liquid and solid phase.

Our second formulation is Taylor-expanded density functional theory, which neglects the density fluctuations with respect to a reference density beyond second order in the free energy formulation. It constitutes already a drastic approximation in density functional theory; nevertheless it is occasionally depicted in the literature as "the" density functional theory from which the third formulation investigated here, the phase-field crystal model of the simplest type, can be derived. In short, the phase-field crystal model can be viewed as a local expansion in density fluctuations and in their gradients of Taylor-expanded density functional theory. The model (see below for its description and references, **b**ut here we want to draw the reader's attention to the very recent review [5]) has lately come to some prominence in the materials science community mainly for the reason alluded to a microscopic foundation of phase-field descriptions (see Ref. [6] for a systematic attempt in that direction).

The paper is structured as follows. Section II introduces briefly the foundations of classical density functional theory and describes the formal approximation steps leading to Taylor-expanded density functionals and phase-field crystal models. In Sec. III, the explicit functionals are given, and they are applied to the hard-sphere system. In calculating surface tensions and the interface structure, no further approximations are made in order to avoid uncertainties in interpreting the results. We concisely discuss the problem of parameter fixing for the phase-field crystal model. Section IV contains our summary and conclusions.

II. DENSITY FUNCTIONAL THEORY AND PHASE-FIELD CRYSTAL MODELS

As discussed before, the phase and the density field in the phase-field formulation should be both obtainable through a suitable coarse graining of the microscopic density field. Thus one may be tempted to forego the artificial distinction between (coarse-grained) phase and (coarse-grained) density field entirely in favor of the microscopic density $\rho(\mathbf{r})$. Indeed, in equilibrium the basic theorems of density functional theory assure us that there is a unique free energy functional of the one-particle density field $\rho(\mathbf{r})$,

$$\mathcal{F}[\rho] = \mathcal{F}^{\mathrm{id}}[\rho] + \mathcal{F}^{\mathrm{ex}}[\rho], \tag{8}$$

$$\text{with} \qquad \beta\mathcal{F}^{\mathrm{id}}[\rho] = \int d^3r \rho(\mathbf{r})[\ln(\rho(\mathbf{r})\Lambda^3) - 1], \tag{9}$$

which can be split into the exactly known ideal gas part $\mathcal{F}^{\mathrm{id}}$ [Λ is the de Broglie wavelength, $\beta = 1/(k_{\mathrm{B}}T)$ is the inverse temperature] and a generally unknown excess part $\mathcal{F}^{\mathrm{ex}}$. The equilibrium density ρ_{eq} in the presence of an external (one-particle) potential $V^{\mathrm{ext}}(\mathbf{r})$ is then given by

$$\left.\frac{\delta\mathcal{F}[\rho]}{\delta\rho(\mathbf{r})}\right|_{\rho=\rho_{\mathrm{eq}}} = \mu - V^{\mathrm{ext}}(\mathbf{r}), \tag{10}$$

where μ is the imposed chemical potential (e.g., by requiring a certain bulk density far away from the region where the external potential acts). For diffusive dynamics, the time evolution of this microscopic one-particle density field obeys the type of dynamics as in Eqs. (1) and (2):

$$\frac{\partial\varrho}{\partial t} = \Gamma\nabla\cdot\left\{\rho(\mathbf{r},t)\nabla\left[\frac{\delta\mathcal{F}[\rho]}{\delta\rho(\mathbf{r},t)} + V^{\mathrm{ext}}(\mathbf{r},t)\right]\right\}. \tag{11}$$

To show this, one needs the possibly severe approximation that the time-dependent density-density correlation function can be approximated by the corresponding equilibrium object, which in turn is obtainable from the equilibrium density functional $\mathcal{F}[\rho]$ [7]. Note that the density field $\rho(\mathbf{r},t)$ is an ensemble-averaged quantity with no coarse-graining in space and time, and there is no noise term in Eq. (11).

A. Functional Taylor expansion

Since the excess free energy functional $\mathcal{F}^{\mathrm{ex}}$ is unknown in general, many practical applications of DFT have started from an expansion of $\mathcal{F}^{\mathrm{ex}}$ around a background reference density

profile $\rho_0(\mathbf{r})$ which, in general, can depend on the position:

$$\beta\mathcal{F}^{\rm ex} = \beta F_0^{\rm ex}[\rho_0] - \int d^3r c^{(1)}(\mathbf{r};\rho_0)\Delta\rho(\mathbf{r}) - \frac{1}{2}\int d^3r d^3r' c^{(2)}(\mathbf{r},\mathbf{r}';\rho_0)\Delta\rho(\mathbf{r})\Delta\rho(\mathbf{r}') + \cdots . \tag{12}$$

Here $F_0^{\rm ex}[\rho_0]$ is the excess free energy pertaining to the background profile, $\Delta\rho(\mathbf{r}) = \rho(\mathbf{r}) - \rho_0(\mathbf{r})$, and $c^{(1)}$ and $c^{(2)}$ are the first two members in the hierarchy of direct correlation functions $c^{(n)}$, defined by

$$c^{(n)}(\mathbf{r}_1,\ldots,\mathbf{r}_n;\rho_0) = -\beta \left.\frac{\delta^{(n)}\mathcal{F}^{\rm ex}}{\delta\rho(\mathbf{r}_1)\cdots\delta\rho(\mathbf{r}_n)}\right|_{\rho=\rho_0(\mathbf{r})} . \tag{13}$$

In most practical applications, $\rho_0 \equiv$ const. is taken to be a reference bulk density, in which case $-c^{(1)} = \beta\mu^{\rm ex} = \beta\mu - \log(\rho_0\Lambda^3)$ and $c^{(2)}(\mathbf{r}-\mathbf{r}';\rho_0)$ depends only on the coordinate difference of the two positions $\mathbf{r}$ and $\mathbf{r}'$. To evaluate the functional in Eq. (12), the correlation function $c^{(2)}$ has to be determined as an external input, provided, e.g., by integral equation theory or by simple approximations of RPA type [8].

It is perhaps somewhat surprising that the functional in Eq. (12) (with ρ_0 being a bulk density) is capable of describing fluid-solid coexistence. This has been shown first in Ref. [9] for the case of hard spheres (for an fcc crystal structure) with $c^{(2)}$ taken to be the analytically known solution of the Percus-Yevick closure to the integral equations. After all, the direct correlation function in the *solid* phase should be very distinct from the one in the *liquid* phase, as can be inferred from the definition in Eq. (13). Consequently the expansion should hold only for modest departures from the reference bulk density, which is not the case when comparing the density distribution in the crystal and the liquid, owing to the occurrence of sharply peaked crystal density profiles. However, the fcc crystal density profile probes the Fourier transform $\tilde{c}^{(2)}(k;\rho)$ at discrete points in k-space [the reciprocal lattice vectors (RLV)], which include the points where the structure factor has its maxima. Furthermore, the **k** vectors of the RLV are distributed fairly isotropically (see also a more detailed discussion in Ref. [10]).

With suitable input for $c^{(2)}$, the Taylor expanded functional in Eq. (12) is also capable of describing the fluid-bcc transition (relevant for the description of, e.g., iron). See Ref. [11] for a recent study. However, the numerical results for free energies and for crystal-liquid surface tensions obtained in such studies do not compare well with simulation results; e.g., the surface tensions from Ref. [11] deviate by a factor of 2. Thus, the Taylor-expanded functional appears to be merely a suitable qualitative tool to explore basic features of dense liquids in the vicinity of the solid or glass transition (see, e.g., Refs. [12,13]).

B. The phase-field crystal model

The Taylor expanded functional in Eq. (12) is nonlocal in the densities. Through an additional approximation (gradient expansion) it can be cast into a local form. We consider again a constant reference density ρ_0 and the following power expansion of the Fourier transform of the direct correlation function:

$$\tilde{c}^{(2)}(k;\rho) = -c_0 + c_2\,k^2 - c_4\,k^4\cdots . \tag{14}$$

Using this, the Taylor-expanded functional becomes

$$\beta\mathcal{F}_{\rm loc}^{\rm ex} = \beta F_0^{\rm ex}(\rho_0) + \beta\mu^{\rm ex}\int d^3r\,\Delta\rho(\mathbf{r}) + \frac{1}{2}\int d^3r\,\Delta\rho(\mathbf{r})(c_0+c_2\nabla^2+c_4\nabla^4\cdots)\Delta\rho(\mathbf{r}) + \cdots . \tag{15}$$

We observe that the excess free energy density contains local terms up to order 2 in $\Delta\rho$ and up to order 4 in $\nabla(\Delta\rho)$. The total free energy contains additionally the ideal gas term, $\mathcal{F}^{\rm id}[\rho]$ from Eq. (9). One may expand also this term in $\Delta\rho$ in order to obtain a consistently power-expanded free energy density. It has been customary in the literature to introduce the dimensionless density difference as an order parameter:

$$\phi(\mathbf{r}) = \frac{\rho(\mathbf{r})-\rho_0}{\rho_0}. \tag{16}$$

In terms of ϕ, the power-expanded total free energy up to order 4 in ϕ and $\nabla\phi$ reads

$$\beta\mathcal{F} \approx \beta F_0(\rho_0) + \int d^3r\left[\rho_0\beta\mu\phi(\mathbf{r}) + \frac{a_{\rm id}\phi^2(\mathbf{r})}{2} - \frac{b_{\rm id}\phi^3(\mathbf{r})}{3} + \frac{g_{\rm id}\phi^4(\mathbf{r})}{4}\right] + \frac{\rho_0^2}{2}\int d^3r\,\phi(\mathbf{r})(c_0+c_2\nabla^2+c_4\nabla^4)\phi(\mathbf{r}). \tag{17}$$

The coefficients $a_{\rm id} = \rho_0$, $b_{\rm id} = \rho_0/2$, and $g_{\rm id} = \rho_0/3$ stem from the expansion of the ideal gas part of the free energy. The reference free energy F_0 contains the ideal gas part by $F_0(\rho_0) = F_0^{\rm ex}(\rho_0) + F^{\rm id}(\rho_0)$. The model defined in Eq. (17) looks like a straightforward extension of standard square-gradient Ginzburg-Landau models. It has been formulated in Ref. [14]; however, earlier work has established the usefulness of such a free energy to describe the transition between a homogeneous and a periodically ordered system [15,16]. For a considerably earlier application to phase transitions in amphiphilic systems, see Ref. [17]. Its central features are:

(1) For $c_2, c_4 > 0$, the term $\propto \phi\nabla^2\phi$ favors a periodically varying ϕ and the term $\propto \phi\nabla^4\phi$ punishes a spatially varying ϕ

(2) Depending on the parameters, it may have as equilibrium states periodically ordered phases in one dimension (stripes), two dimensions (rods), and three dimensions (bcc, fcc, hcp)

(3) The characteristic wave number of the order parameter field is $q_0 = \sqrt{c_2/(2c_4)}$, which follows from

$$\phi(\mathbf{r})(c_2\nabla^2 + c_4\nabla^4)\phi(\mathbf{r}) = \phi(\mathbf{r})\left[-c_4 q_0^4 + c_4\left(q_0^2+\nabla^2\right)^2\right]\phi(\mathbf{r}).$$

It turns out that the phase diagram of the above model is equivalent to the formulation of a reduced model with the free energy according to [18]

$$F_{\rm PFC} = \int d^3x f_{\rm PFC} = \int d^3x\left\{\Psi(\mathbf{x})[-\epsilon + (1+\nabla)^2]\Psi(\mathbf{x}) + \frac{\Psi(\mathbf{x})^4}{4}\right\}, \tag{18}$$

which we call the (actual) phase-field crystal (PFC) model. Indeed, we can define the dimensionless coordinate $\mathbf{x}$, a free energy scale E_0, and the reduced field Ψ through the transformations

$$\mathbf{x} = q_0\mathbf{r} = \sqrt{\frac{c_2}{2c_4}}\mathbf{r}, \quad E_0 = \frac{\rho_0^4 c_4^2 q_0^5}{g_{\mathrm{id}}}, \qquad \Psi = \sqrt{\frac{g_{\mathrm{id}}}{\rho_0^2 c_4 q_0^4}}\left(\Phi - \frac{b_{\mathrm{id}}}{3g_{\mathrm{id}}}\right), \tag{19}$$

and the free energy in Eq. (17) becomes

$$\beta\mathcal{F} = E_0 \int d^3x \, (B_0 + B_1\Psi(\mathbf{x}) + f_{\mathrm{PFC}}) \tag{20}$$

with the value of ϵ [see Eq. (18) for the definition of f_{PFC}] given by

$$\epsilon = \frac{1}{\rho_0^2 c_4 q_0^4}\left[- a_{\mathrm{id}} - \rho_0^2\left(c_0 - c_4 q_0^2\right) + \frac{b_{\mathrm{id}}^2}{3g_{\mathrm{id}}}\right]. \tag{21}$$

The constants B_0 and B_1 are given by

$$B_0 = \frac{108 g_{\mathrm{id}}^3 \beta F_0 + 36 g_{\mathrm{id}}^2 b_{\mathrm{id}} \rho_0 \beta\mu + b_{\mathrm{id}}^2\left(6 a_{\mathrm{id}} g_{\mathrm{id}} - b_{\mathrm{id}}^2 + 6 g_{\mathrm{id}}\rho_0^2 c_0\right)}{108 g_{\mathrm{id}}^2 q_0^8 \rho_0^4 c_4^2}, \tag{22}$$

$$B_1 = \sqrt{\rho_0^2 c_4 q_0^4 g_{\mathrm{id}}}\, \frac{27 g_{\mathrm{id}}^2 \rho_0 \beta\mu + b_{\mathrm{id}}\left(9 a_{\mathrm{id}} g_{\mathrm{id}} - 2 b_{\mathrm{id}}^2 + 9 g_{\mathrm{id}}\rho_0^2 c_0\right)}{27 g_{\mathrm{id}}^2 q_0^8 \rho_0^4 c_4^2}. \tag{23}$$

The term $B_0 + B_1\Psi$ in the free energy Eq. (20) does not influence the location of the phase boundaries since it is linear only in Ψ, but it affects the values of the free energy density and the chemical potential at coexistence. Since we will determine these values explicitly later, we have given the expressions for B_0 and B_1 explicitly. Thus the phase diagram is determined by the variables occurring in f_{PFC}, i.e., only by the parameter ϵ and $\bar{\Psi}$, the average value of $\Psi(\mathbf{x})$. The associated phase diagram has been calculated in Ref. [18] and is depicted in Fig. 1.

In the next section, we turn to an exemplification of DFT, Taylor-expanded DFT, and PFC for the hard-sphere system. In particular, we will examine minimized solutions for crystals and values for crystal-liquid coexistence and crystal-liquid surface tensions as well as interfacial profiles for density modes. It will turn out that the apparent straightforwardness of the PFC derivation from Taylor-expanded DFT is misleading and cannot be upheld, if one likes to describe crystals with PFC.

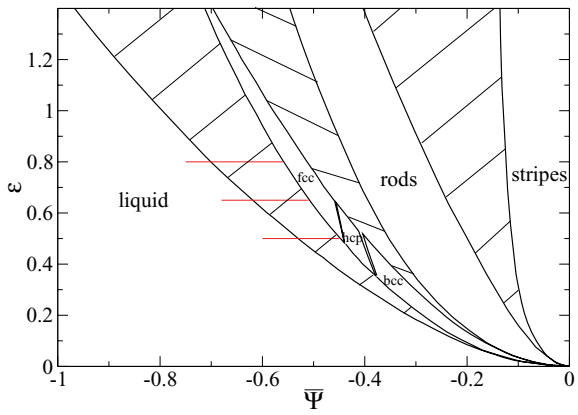

FIG. 1. (Color online) Phase diagram of the PFC free energy (18). $\bar{\Psi}$ denotes the average order parameter in the bulk phase. Data are taken from Ref. [18]. The horizontal lines mark the values $\epsilon = 0.5$, 0.65, and 0.8 for which explicit results are discussed (see below).

III. RESULTS FOR HARD SPHERE CRYSTALS AND CRYSTAL-LIQUID INTERFACE

A. DFT: fundamental measure theory

For hard spheres, fundamental measure theory (FMT) allows the construction of very precise functionals [19–22]. Essentially FMT postulates an excess free energy with a local free energy density expressed in a set of weighted densities n_α:

$$\mathcal{F}^{\mathrm{ex}}[\rho] = \int d^3r \, \Phi[n_\alpha(\mathbf{r})]. \tag{24}$$

The weighted densities are constructed as convolutions of the density with weight functions, $n_\alpha(\mathbf{r}) = \rho * w^\alpha(\mathbf{r})$. The weight functions reflect the geometric properties of the hard spheres. For one species, the weight functions include four scalar functions $w^0, \ldots, w^3$, two vector functions $\mathbf{w}^1, \mathbf{w}^2$, and a tensor function w^t defined as

$$\begin{aligned} w^3 &= \theta(R - |\mathbf{r}|), \quad w^2 = \delta(R - |\mathbf{r}|), \\ w^1 &= \frac{w^2}{4\pi R}, \quad w^0 = \frac{w^2}{4\pi R^2}, \\ \mathbf{w}^2 &= \frac{\mathbf{r}}{|\mathbf{r}|}\delta(R - |\mathbf{r}|), \quad \mathbf{w}^1 = \frac{\mathbf{w}^2}{4\pi R}, \\ w^t_{ij} &= \frac{r_i r_j}{\mathbf{r}^2}\delta(R - |\mathbf{r}|). \end{aligned} \tag{25}$$

Here $R = \sigma/2$ is the hard-sphere radius. Using these weight functions, corresponding scalar weighted densities $n_0, \ldots, n_3$, vector weighted densities $\mathbf{n}_1, \mathbf{n}_2$, and one tensor weighted density n_t are defined. In constructing the free energy density Φ, arguments concerning the correlations in the bulk fluid and arguments for strongly inhomogeneous systems are used (for reviews see Refs. [21,22]). For the bulk, Φ is required to reproduce exactly the second and third virial coefficent of the direct correlation function. Furthermore, consistency with a scaled particle argument and/or imposition of the Carnahan-Starling equation of state leads to the following form of

the excess free energy density [22]:

$$\Phi(\{\mathbf{n}[\rho(\mathbf{r})]\}) = -n_0 \ln(1-n_3) + \varphi_1(n_3)\,\frac{n_1 n_2 - \mathbf{n}_1\cdot\mathbf{n}_2}{1-n_3} + \varphi_2(n_3)\,\frac{3(-n_2\,\mathbf{n}_2\cdot\mathbf{n}_2 + n_{2,i}n_{t,ij}n_{2,j} + n_2\,n_{t,ij}n_{t,ji} - n_{t,ij}n_{t,jk}n_{t,ki})}{16\pi(1-n_3)^2}. \tag{26}$$

Here $\varphi_1(n_3)$ and $\varphi_2(n_3)$ are functions of the local packing density $n_3(\mathbf{r})$. With the choice

$$\varphi_1 = 1 \quad \text{and} \quad \varphi_2 = 1 \tag{27}$$

we obtain the Tarazona tensor functional [20], which is built upon the original Rosenfeld functional [19]. The latter gives the fluid equation of state and pair structure of the Percus-Yevick approximation. Upon setting

$$\varphi_1 = 1 + \frac{2n_3 - n_3^2 + 2(1-n_3)\ln(1-n_3)}{3n_3},$$
$$\varphi_2 = 1 - \frac{2n_3 - 3n_3^2 + 2n_3^3 + 2(1-n_3)^2\ln(1-n_3)}{3n_3^2}, \tag{28}$$

we obtain the tensor version of the recently introduced White Bear II (WBII) functional [23].

For bulk crystals, very accurate free energy results can already be obtained using a Gaussian approximation for the density,

$$\rho(\mathbf{r}) = \sum_{\text{lattice sites } i} (1-n_{\text{vac}})\left(\frac{\alpha}{\pi}\right)^{\frac{3}{2}} \exp[-\alpha(\mathbf{r}-\mathbf{r}_i)^2/\sigma^2], \tag{29}$$

and minimizing the total free energy with respect to the width parameter α and the vacancy concentration n_{vac} at a fixed bulk density. At coexistence $\alpha \sim 80$, in accordance with simulations and free energies per particle between Gaussian parametrized DFT and simulations agree on the level of 0.01 $k_B T$ [10]. However, the Tarazona functional (27) yields $n_{\text{vac}} \to 0$, while the WBII functional Eq. (28) gives a finite equilibrium vacancy concentrations $n_{\text{vac}} = O(10^{-5})$, which is about a factor 10 smaller than in the simulation results [26]. This fine difference has important consequences: performing an unconstrained minimization [see Eq. (10) with vanishing external potential] only the WBII functional gives an absolute minimum for the free energy with a value for the chemical potential which is consistent with the derivative of the crystal free energy density with respect to the bulk density (see Ref. [10] for further details). This implies that a free minimization for the crystal-fluid interface can only be performed using the WBII functional.

The free minimization of the crystal-fluid interface is a nontrivial task; a brief description of the method (also applicable in the case of Taylor-expanded DFT) is given in Appendix A. Results for the surface tension with crystal faces in different orientations have been reported in Ref. [27] and are also given in Table I. There is agreement with simulations in the ordering $\gamma_{[100]} > \gamma_{[110]} > \gamma_{[111]}$ and as far as the accuracy of the data permits also in the values of the relative anisotropies [i.e., the values of $(\gamma_{[100]} - \gamma_{[110]})/\gamma_{[100]}$ and $(\gamma_{[100]} - \gamma_{[111]})/\gamma_{[100]}$]. There is no clear consensus between different simulation methods on the absolute values of γ, but the latest results are closer to the DFT values, however.

Overall these results corroborate what is known from many applications of FMT on (dense) liquids [22,29,30]: It is a quantitative theory, and the accuracy also extends to the description of crystalline systems. Therefore we can consider FMT as a benchmark theory against which subsequent approximative approaches should be tested.

B. Taylor-expanded DFT

We consider the Taylor-expanded functional Eq. (12) of the FMT functionals, Eq. (27) (Tarazona functional), and Eq. (28)

TABLE I. Results for coexistence properties and crystal-fluid surface tension using the different approaches considered in this work. The PFC results have been obtained using the fitting procedure described in Sec. III C for the reference density $\rho_0\sigma^3 = 0.94$ with the crystal and fluid coexistence densities as input (in italics).

	FMT (WBII)	T–DFT (PY)	T–DFT (WBII)		PFC		SIM		
$\rho_0\sigma^3$		0.9461	1.026		0.94				
ϵ				0.50	0.65	0.80			
$\rho_{\text{cr}}\sigma^3$	1.039	1.049	1.123		*1.04*		1.041 [24]	1.039 [25]	
$\rho_{\text{fl}}\sigma^3$	0.945	0.944	1.021		*0.94*		0.940 [24]	0.938 [25]	
$(\beta F/N)_{\text{cr}}$	4.96	5.33	7.23		5.20		4.96[a]		
$(\beta F/N)_{\text{fl}}$	3.82	3.99	5.05		3.93		3.75[b]		
$\beta\mu_{\text{coex}}$	16.38	17.44	21.51		17.16		16.09[b]		
n_{vac}	2×10^{-5}	0.10	0.09	−0.11	−0.12	−0.13	3×10^{-4} [26]		
$\beta\sigma^2\gamma_{[100]}$	0.69 [27]	0.89	1.31	0.140	0.074	0.046	0.58 [25]	0.63 [27]	0.64 [28]
$\beta\sigma^2\gamma_{[110]}$	0.67	0.85	1.21	0.132	0.070	0.043	0.56	0.61	
$\beta\sigma^2\gamma_{[111]}$	0.64	0.78	1.09	0.105	0.055	0.034	0.54	0.60	

[a]Free energy for $\rho_{\text{cr}}\sigma^3 = 1.041$ [24] using an improved fit in the form of the Speedy equation of state from Ref. [10].
[b]Free energy and chemical potential for $\rho_{\text{fl}}\sigma^3 = 0.940$ [24] from the Carnahan-Starling equation of state.

(WBII functional). The nontrivial, second-order term in the functional involves the direct correlation function $c^{(2)}(r;\rho_0)$. It is the second derivative of the excess free energy functional and is given in both cases by the polynomial form

$$c^{(2)}(r;\rho_0) = [a_1 + a_2 r/\sigma + a_3 (r/\sigma)^3]\theta(\sigma - r). \quad (30)$$

Using the packing fraction $\eta = \pi\sigma^3/6\,\rho_0$, the coefficients for $c^{(2)}$ of the Tarazona functional are those of the famous Percus-Yevick solution,

$$a_1 = -\frac{(1+2\eta)^2}{(1-\eta)^4}, \quad a_2 = 6\eta\frac{(1+\eta/2)^2}{(1-\eta)^4} \quad \text{(Tarazona)}, \qquad a_3 = \frac{\eta}{2}a_1. \quad (31)$$

The coefficients for $c^{(2)}$ of the WBII functional are given by

$$a_1 = -\frac{1+4\eta+4\eta^2-4\eta^3+\eta^4}{(1-\eta)^4},$$
$$a_2 = \frac{-2+25\eta+12\eta^2-10\eta^3+2\eta^4}{3(1-\eta)^4} + \frac{2\ln(1-\eta)}{3\eta} \quad \text{(White Bear II)}, \quad (32)$$
$$a_3 = \frac{1-4\eta+2\eta^2-3\eta^3+\eta^4}{(1-\eta)^4} + \frac{\ln(1-\eta)}{\eta}.$$

Both forms approximate the simulation results for $c^{(2)}$ reasonably well (see Fig. 2), with the WBII form matching more closely. As we will see, this does *not* imply better results for the Taylor-expanded functional in the WBII case.

The Taylor-expanded functional contains the reference density ρ_0 as an additional parameter. It would be desirable to choose it such that it also recovers the fluid density at coexistence. In this way it is guaranteed that at least the fluid properties are almost exact if the Taylor-expanded functional is fixed adequately. In order to determine ρ_0 with moderate effort, we employ the approach already taken in Ref. [32]. For a given bulk density ρ_b, we parametrize the density profile in the Gaussian form Eq. (29) and determine the three free parameters α (Gaussian width), n_{vac} (vacancy concentration), and ρ_0 by minimizing the functional for the grand potential *difference* per particle between crystal and liquid at the chemical potential $\mu(\rho_0)$:

$$\frac{\beta\Delta\Omega(\rho_b)}{N} = \min_{\alpha,n_{vac},\rho_0}\left\{\frac{1}{\rho_b V}\int_V d^3r\left[\rho(\mathbf{r})\ln\frac{\rho(\mathbf{r})}{\rho_0} - \rho(\mathbf{r}) + \rho_0\right] - \frac{1}{2\rho_b V}\int_V d^3r\,d^3r'\,c^{(2)}(\mathbf{r},\mathbf{r}';\rho_0)\Delta\rho(\mathbf{r})\Delta\rho(\mathbf{r}')\right\}, \quad (33)$$

where $\Delta\rho(\mathbf{r}) = \rho(\mathbf{r}) - \rho_0$ is defined as before. In practice, the space integrations can be restricted to one cubic fcc unit cell. Finally, the bulk density ρ_b is varied until $\Delta\Omega(\rho_b) = 0$; i.e., at this point ρ_b and ρ_0 (from the minimization) correspond to the coexisting crystal and fluid densities within the Gaussian approximation. We pick this ρ_0 as the reference density for the unconstrained minimization, and redetermine the bulk crystal and fluid densities at coexistence through a full minimization and a subsequent Maxwell construction. These densities are only slightly shifted from the ones obtained within the Gaussian approximation (see Table I).

The results are partially surprising (see Table I). For the Taylor-expanded Tarazona functional (i.e., employing the $c^{(2)}$ of Percus-Yevick), the coexisting densities are still very close to the simulation and FMT (0.944 and 1.049). In the Gaussian approximation, similar values have been already obtained in 1985 by Jones and Mohanty [32]. The crystal free energy is too big ($\beta F/N = 5.33$ vs 4.96 from simulation and FMT), and the width of the Gaussian peaks is much too narrow ($\alpha \sim 600$ vs 80 from simulation and FMT). For the WBII functional (i.e., the better functional, with a more precise $c^{(2)}$) the coexistence densities are considerably off (1.021 and 1.123); consequently the crystal free energy is too big by 40%, and the Gaussian width parameter $\alpha \sim 1000$ stands for even narrower peaks. For both functionals, the vacancy concentrations are too large by three orders of magnitude.

As before for FMT, we determine the surface tensions using a full minimization (see Appendix A). It is gratifying that the ordering $\gamma_{[100]} > \gamma_{[110]} > \gamma_{[111]}$ is upheld, but the relative anisotropies are too large by approximately a factor of 2 and the average value of the surface tension is too large [Taylor-expanded Tarazona functional: 0.84, Taylor-expanded White Bear II functonal: 1.2 vs 0.67 from full FMT, all values in units of $1/(\beta\sigma^2)$].

In conclusion, it is apparent that through Taylor expansion of the precise FMT functionals, crystal free energies, surface tensions, and vacancy concentrations are severely affected. Nevertheless, a qualitative description is still achieved. The reason for the quantitative failure of the Taylor-expanded functionals is most likely due to the fact that the packing constraints or free energies for highly localized states are not respected very well. This is in contrast to the FMT functionals which have incorporated the correct description of localized states [20,21].

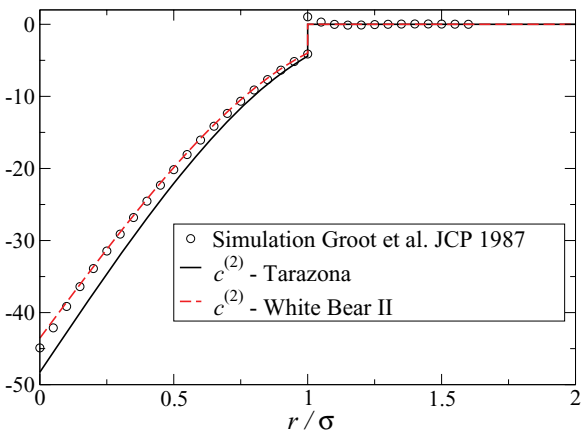

FIG. 2. (Color online) Direct correlation function for hard spheres at a density $\rho\sigma^3 = 0.9$, somewhat below freezing. Simulation data are taken from Ref. [31].

C. Phase-field crystal modelling

1. Fixing parameters using bulk properties

From the phase diagram of the PFC model (Fig. 1) with free energy density

$$f_{\mathrm{PFC}} = \Psi(\mathbf{x})[-\epsilon + (1+\nabla)^2]\Psi(\mathbf{x}) + \frac{\Psi(\mathbf{x})^4}{4},$$

one infers that, for the description of stable fluid-crystal(fcc) coexistence, a parameter range of $\epsilon \sim 0.5, \ldots, 1$ is necessary. For lower ϵ, fcc is metastable only with respect to bcc, and for $\epsilon < 0$ there are no ordered phases at all. However, following the derivation of PFC from the Taylor-expanded functional, one is led to the free energy in Eq. (17) with coefficients a_{id}, b_{id}, g_{id} from the expansion of the ideal gas free energy and the Taylor coefficients c_0, c_2, c_4 from the expansion of the Fourier transform of the direct correlation function $\tilde{c}^{(2)}(k;\rho)$. Using the explicit form for $c^{(2)}(r) = a_1 + a_2(r/\sigma) + a_3(r/\sigma)^3$ $(r/\sigma < 1)$, we find

$$\begin{aligned} c_0 &= 4\pi\left(\frac{a_1}{3} + \frac{a_2}{4} + \frac{a_3}{6}\right), \\ c_2 &= \frac{4\pi}{6}\left(\frac{a_1}{5} + \frac{a_2}{6} + \frac{a_3}{8}\right), \\ c_4 &= \frac{4\pi}{120}\left(\frac{a_1}{7} + \frac{a_2}{8} + \frac{a_3}{10}\right), \end{aligned} \tag{34}$$

and inserting into the equation (21) for ϵ we obtain $\epsilon = -0.6 \cdots - 0.7$ ($\rho_0\sigma^3 = 0.94, \ldots, 1.04$, Percus-Yevick direct correlation function). Thus, the naive gradient expansion of the Taylor-expanded functional produces a free energy which shows no sign of a liquid-solid transition. The reason is essentially that the gradient expansion roughly approximates the Fourier transform of the direct correlation function $\tilde{c}^{(2)}(k;\rho)$ and consequently also the structure factor defined by

$$S(k;\rho) = \frac{1}{1 - \rho\tilde{c}^{(2)}(k;\rho)}. \tag{35}$$

The gradient expansion leads to a structure factor which clearly violates the empirical Verlet-Hansen freezing criterion [height of first peak in $S(k) \gtrsim 2.8$], whereas $S(k)$ from the PY direct correlation function fulfills it.

Such a failure of the naive gradient expansion has been noted and discussed before in a case study on the applicability of PFC for bcc metals [11]. The remedy proposed was to fit c_0, c_2, c_4 to the first maximum of $\tilde{c}^{(2)}(k;\rho)$ [or $S(k;\rho)$] at around $k\sigma \sim 7$ and also to fit the coefficients a_{id}, b_{id}, g_{id} in order to achieve a reasonable description of coexistence. The results from this procedure can be considered as partially successful: The correct description of the first peak of the structure factor needs a value for c_0 which is too small and hence causes deviations of the liquid isothermal compressibility $\beta(\partial p/\partial\rho)^{-1} = 1/[1 - \rho\tilde{c}^{(2)}(0;\rho)] = S(0;\rho)$. Also, bulk free energies are not well captured [11].

Another serious problem is related to the identification of the order parameter $\Phi(\mathbf{r}) = \rho(\mathbf{r})/\rho_0 - 1$ [see Eq. (17)] with the shifted dimensionless density. The order parameter Ψ of the PFC model is related to a rescaling and shift of the order parameter ϕ. Numerical solutions of the PFC model for $\epsilon > 0$ show that the order parameter solutions for bulk crystals can still be approximated by Gaussians [Eq. (29)], but they are much more spread out (width parameter $\alpha \sim 10$, compared to 80 (for the case of FMT) and 500...1000 (for the case of Taylor-expanded DFT). Consequently $\Phi(\mathbf{r})$ has to be interpreted rather as a smeared-out reduced density. We will model this idea using a simple, normalized Gaussian smearing function with width α' leading to the following reinterpretation of $\Phi(\mathbf{r})$:

$$\Phi(\mathbf{r}) = \frac{\bar{\rho}(\mathbf{r})}{\rho_0} - 1, \tag{36}$$

$$\text{with} \quad \bar{\rho}(\mathbf{r}) = \int d\mathbf{r}' \left(\frac{\alpha'}{\pi}\right)^{\frac{3}{2}} \exp(-\alpha' r'^2/\sigma^2)\rho(\mathbf{r} - \mathbf{r}'). \tag{37}$$

Inserting this ansatz into the approximative free energy in Eq. (17) and applying $c^{(2)} = -\delta^2\mathcal{F}^{\mathrm{ex}}/(\delta\rho\delta\rho)$, we find the following Fourier transform for the direct correlation function:

$$\tilde{c}^{(2)}(k;\rho) = \exp\left(-\frac{k^2}{2\alpha'}\right)(-c_0 + c_2k^2 - c_4k^4 \cdots). \tag{38}$$

Treating α', c_0, c_2, c_4 as fitting parameters, we obtain very accurate fits of *both*, $\tilde{c}^{(2)}(k;\rho)$ and $S(k)$ in the "long wavelength" region $k\sigma \lesssim 10$ for different choices of the reference density ρ_0, see Fig. 3 and Table II. The good matching properties are

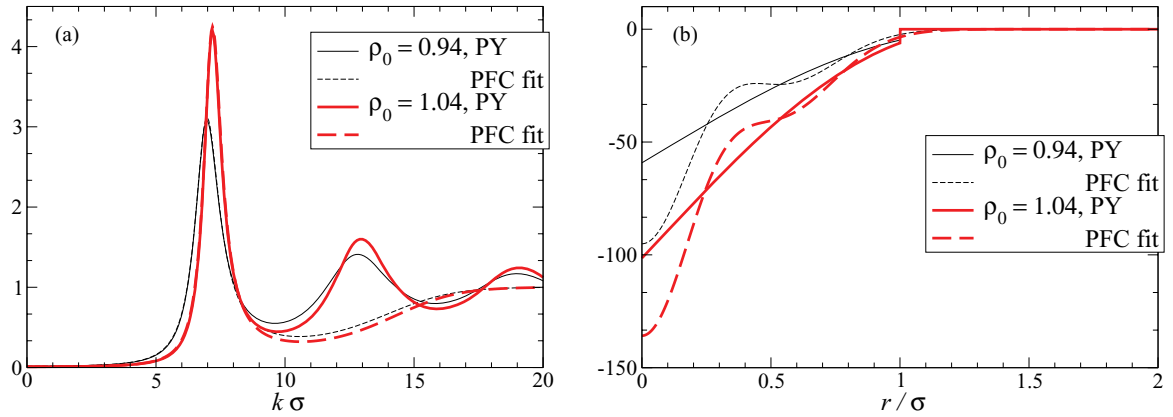

FIG. 3. (Color online) Comparison between Percus-Yevick results (full lines) and PFC fits (dashed lines). (a) Structure factor $S(k;\rho_0)$. (b) Direct correlation function $c^{(2)}(r;\rho_0)$. Thin lines are for a reference density $\rho_0\sigma^3 = 0.94$ and thick lines for $\rho_0\sigma^3 = 1.04$.

TABLE II. PFC fitting parameters and results for the bulk liquid and crystal phases at coexistence.

$\rho_0\sigma^3$	ϵ	α'	$c_0\sigma^3$	$c_2\sigma^5$	$c_4\sigma^7$	$a\sigma^3$	$b\sigma^3$	$g\sigma^3$	E_0	$\left(\frac{\beta F}{N}\right)_{\mathrm{cr}}$	$\left(\frac{\beta F}{N}\right)_{\mathrm{fl}}$	$\beta\mu_{\mathrm{coex}}$	n_{vac}
Simulation										3.75	4.96	16.1	10^{-4}
0.94	0.5	14.21	61.93	2.567	0.0249	23.45	69.75	33.13	0.279	3.93	5.20	17.16	−0.11
	0.65					32.40	112.0	62.75	0.147	3.93	5.20	17.16	−0.12
	0.8					42.02	160.5	101.0	0.091	3.93	5.20	17.16	−0.13
1.0	0.5	13.93	80.36	3.201	0.03013	21.04	98.19	54.57	0.342	3.99	5.06	15.06	−0.06
	0.65					26.75	154.9	103.4	0.181	4.01	5.01	14.48	−0.07
	0.8					32.42	218.6	166.3	0.112	4.02	4.97	13.90	−0.08
1.04	0.5	13.99	96.56	3.745	0.03458	16.58	122.9	76.15	0.397	4.11	4.94	12.77	−0.03
	0.65					18.40	191.1	144.2	0.209	4.15	4.89	11.92	−0.04
	0.8					19.53	266.5	232.1	0.130	4.18	4.84	11.07	−0.05

a result of the fit with $\alpha' \approx 14$. This value naturally accounts for the extended width of the bulk crystal solutions for $\Phi(\mathbf{r})$. Additionally we also have the qualitatively correct behavior for $c^{(2)}(r)$ for *short* distances $r \lesssim \sigma$ (see Fig. 3). Furthermore, in line with the previous studies [11,33], we treat the coefficients $a_{\mathrm{id}}, b_{\mathrm{id}}, g_{\mathrm{id}} \to a, b, g$ as free parameters since the ideal gas free energy cannot be applied to a smoothed density field $\bar{\rho}$ as defined above. A direct way to fix these parameters is by using the physical hard-sphere coexistence densities ρ_{cr} and ρ_{fl} as input. Since the PFC phase diagram is described by the reduced PFC free energy in Eq. (18) (see Fig. 1), the triple $\epsilon, \bar{\Psi}_{\mathrm{cr}}(\epsilon), \bar{\Psi}_{\mathrm{fl}}(\epsilon)$ fixes the three coefficients a, b, g using the third relations of Eqs. (19) and (21). Here $\bar{\Psi}_{\mathrm{cr}}(\epsilon)$ and $\bar{\Psi}_{\mathrm{fl}}(\epsilon)$ are the coexistence values for the average order parameter of the fcc crystal and of the fluid, respectively.

In summary, a reasonable procedure to fix the PFC parameters is as follows:

(1) Fix a reference density ρ_0, fit $S(k; \rho_0) = 1/[1 - \rho_0 \tilde{c}^{(2)}(k; \rho_0)]$ using Eq. (38) in the wave vector region including the first peak of the structure factor ($k\sigma \lesssim 10$).

(2) Fix the PFC parameter ϵ and require coexistence at the physical coexistence densities: This determines a, b, g and consequently also the length scale q_0 and the free energy scale E_0 of the PFC model.

We have gathered the results of this procedure for some combinations of reference densities and ϵ parameters in Table II. Note that the fitted values of a, b, g are one to two orders of magnitude larger than the ideal gas values $a_{\mathrm{id}} = \rho_0$, $b_{\mathrm{id}} = \rho_0/2$, $g_{\mathrm{id}} = \rho_0/3$. This is a consequence of the fact that the PFC order parameter should be considered as a smeared-out density.

In Table II we also give the free energy per particle for the coexisting bulk liquid and crystal phases, their chemical potential, and the vacancy concentration of the coexisting crystal, obtained from a minimization of the PFC free energy of Eq. (18) for bulk crystal states. For the absolute values of the free energy and the coexisting chemical potential, one needs to determine the constant and linear terms in the PFC order parameter Ψ (see Eq. (20)). We find that, for the reference density $\rho_0\sigma^3 = 0.94$, the coexistence free energies and the chemical potential are well recovered in this case $\rho_0 = \rho_{\mathrm{fl}}$, the liquid free energy and the chemical potential are those of the PY theory and are hence reasonably accurate. The good approximation of the crystal-fluid free energy difference is in contrast to the findings in Ref. [11].

However, the order parameter profiles Ψ from FMT and PFC in the crystal unit cell at coexistence agree only qualitatively; see Fig. 4. Here the FMT solution for Ψ is calculated

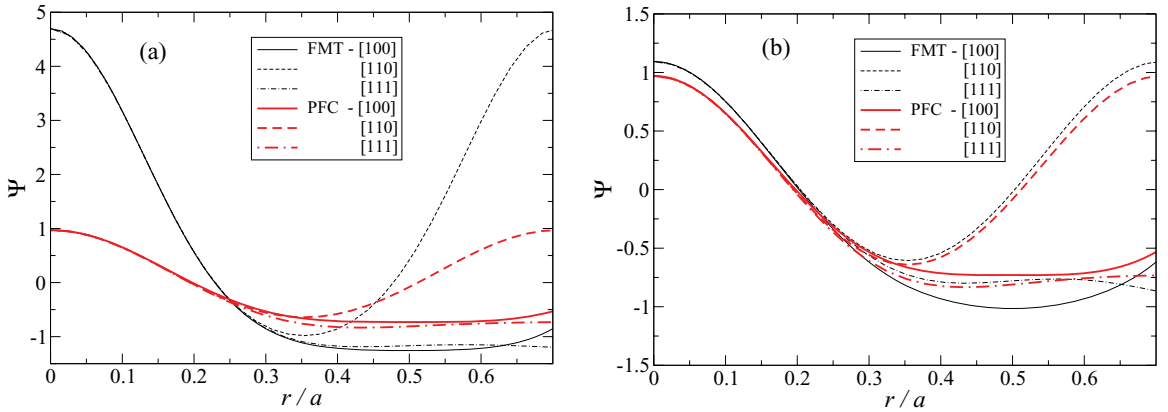

FIG. 4. (Color online) Comparison between FMT (thin lines) and PFC (thick lines) for the order parameter Ψ in the bulk crystal at coexistence, for three different lattice directions in the fcc cubic unit cell of side length a. The order parameter is calculated from the FMT density profile $\rho(\mathbf{r})$ by $\Psi(\mathbf{r}) = \sqrt{g/(\rho_0^2 c_4 q_0^2)}[\bar{\rho}(\mathbf{r})/\rho_0 - 1 - b/(3g)]$ with $q_0^2 = c_2/(2c_4)$ and $\bar{\rho}(\mathbf{r})$ given by the convolution in Eq. (37). Values for b, g, c_2, c_4 are obtained for the data set $\rho_0\sigma^3 = 0.94$ and $\epsilon = 0.5$ (see Table II), and the smearing width for $\bar{\rho}$ is $\alpha' = 14.0$ in (a) and $\alpha' = 7.0$ in (b).

via the third expression of Eq. (19), but with the smeared density profile defined in Eq. (37). Using a smearing parameter $\alpha' = 14.0$, consistent with the structure factor fit in Table II, yields order parameters that vary more strongly in FMT than in PFC [Fig. 4(a)]. Although in Fig. 4(a) the comparison is shown only for one choice of ρ_0 and ϵ, the differences between FMT and PFC are also found for other parameter combinations. Only by choosing $\alpha' = 7.0$ (stronger smearing) do the order parameter profiles agree almost quantitatively [see Fig. 4(b)]. For such low values of α', the fitting procedure gives too large values for the inverse PFC length scale q_0 and too small values for the free energy scale E_0. Thus, the order parameter description in PFC is somewhat defective.

The relative vacancy concentration $n_{\rm vac}$ can be calculated via the number of particles $N_{\rm cell} = \rho_{\rm cr}(a_{\rm min}/q_0)^3$ in the fcc cubic unit cell by $n_{\rm vac} = 1 - N_{\rm cell}/4$. Here $a_{\rm min}$ is the cubic unit cell length in dimensionless PFC units, which follows from minimizing the PFC free energy density at the value for the average order parameter $\bar{\Psi}$ at coexistence. The resulting $n_{\rm vac}$ is negative (see Table II) and of order 0.1, which implies a considerable concentration of interstitial particles. This is, of course, unphysical, but it simply follows from fixing PFC coexistence to the correct physical densities. This observation reflects once more the difficulties in fixing parameters. Similarly to the case of the Taylor-expanded functional, it cannot be expected that a "generic" free energy functional like the PFC functional can capture the correlations in the nearest-neighbor shell of a crystalline particle correctly, especially the condition of no overlap between particles. These correlations determine the precise value of $n_{\rm vac}$.

2. Crystal-fluid surface tensions

We have determined the equilibrium order parameter profile and the associated PFC free energy for the crystal-fluid interface as the long-time limit of the solution to the dynamic equation

$$\frac{\partial \Psi(\mathbf{x},t)}{\partial t} = \nabla^2 \frac{\delta F_{\rm PFC}}{\delta \Psi(\mathbf{x},t)} \tag{39}$$

[see Eqs. (1) and (2)], with initial conditions given by a trial profile for a crystal slab in the simulation box filled otherwise with liquid. Any mobility coefficient, relating the PFC time t in the above equation to real time, is unimportant for the discussion of equilibrium properties. The order parameter profiles and the PFC free energy can be converted to density profiles and physical free energies using Table II. We have noted a certain sensitivity of the surface tensions and the order parameter profiles to the grid spacing and the precise extensions of the simulation box. These details are discussed in Appendix B.

We have calculated the dimensionless PFC surface tension $\hat{\gamma}$ for the three different orientations [100], [110], and [111], each for the values of the PFC parameter $\epsilon = 0.5$, 0.65, and 0.8. In this sequence of orientations the results are 0.0097, 0.0092, 0.0073 ($\epsilon = 0.5$), 0.0132, 0.0129, 0.0102 ($\epsilon = 0.65$), and 0.0165, 0.0163, 0.0129 ($\epsilon = 0.8$). The conversion to physical surface tensions of the hard-sphere system is given by $\gamma = \hat{\gamma} q_0^2 E_0$ with the free energy scale E_0 and the inverse length scale squared $q_0^2 = c_2/(2c_4)$ given in Table II. This results in different γ for different reference densities ρ_0, which

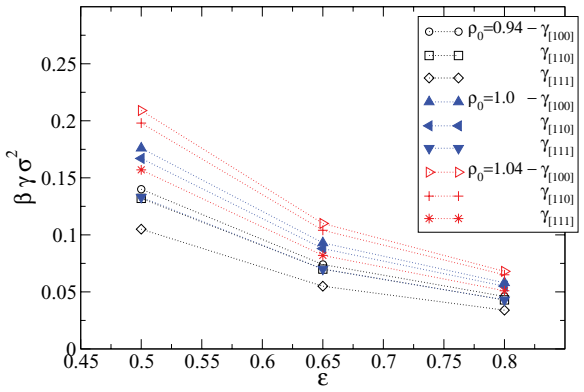

FIG. 5. (Color online) Surface tension from the PFC model for different orientations and different reference densities ρ_0. For different ρ_0, the physical surface tensions $\gamma = \hat{\gamma} q_0^2 E_0$ differ since the free energy scale E_0 and the inverse length scale squared $q_0^2 = c_2/(2c_4)$ differ (see Table II). The dimensionless PFC surface tension $\hat{\gamma}$ is only a function of ϵ (values given in text).

are depicted in Fig. 5. For the reference density $\rho_0\sigma^3 = 0.94$ (where PFC bulk crystal data are in good agreement with FMT and simulation) the surface tension values are given in Table I as well. The physical surface tensions are largest for highest reference density ρ_0 and the lowest PFC parameter ϵ and decrease for decreasing ρ_0 and/or increasing ϵ. Still, on average for the three different orientations the surface tensions are too low compared to FMT/simulation values between a factor of about 3 ($\rho_0\sigma^3 = 1.04$, $\epsilon = 0.5$) and about 15 ($\rho_0\sigma^3 = 0.94$, $\epsilon = 0.8$). The ordering of surface tensions $\gamma_{[100]} > \gamma_{[110]} > \gamma_{[111]}$ is correct for the PFC results but $\gamma_{[111]}$ is smaller than $\gamma_{[100]}$ by about 30%, which differs considerably from the 5%,...,8% as found in simulation and FMT. Likewise a strong qualitative difference between the order parameter profiles of the [111] interface compared to the [100], [110] interfaces is also found: The width of the [111] interface is considerably wider than of the [100], [110] interfaces (see below). This feature is not present in FMT.

D. Density and order parameter modes at the crystal-fluid interface

1. General theory and previous FMT results

Consider a generic field $\psi(x,y,z)$ which describes the crystal-fluid interface with interface normal in the z direction. In DFT, this field is the density $\rho(x,y,z)$ and in PFC, it is the order parameter field $\Psi(x,y,z)$. We can parametrize the field ψ in terms of a modified Fourier expansion

$$\psi(x,y,z) = \sum_j \exp(\mathrm{i}\mathbf{K}_j \cdot \mathbf{r})\ p_j(z), \tag{40}$$

where $\mathbf{K}_j$ denotes the reciprocal lattice vector (RLV), and j- and the z-dependent Fourier amplitude $p_j(z)$ are modes of the field. One expects that upon crossing the interface from the crystal side, all $p_j(z)$ relax to zero for nonzero $\mathbf{K}_j$. Only for $\mathbf{K}_j \equiv 0$, does the value for the associated mode cross from the average field $\bar{\psi}$ of the crystal to the average field of the fluid. It is convenient to group the $\mathbf{K}_j$ in shells with index m, where all $\mathbf{K}_j$ belonging to one shell can be transformed into

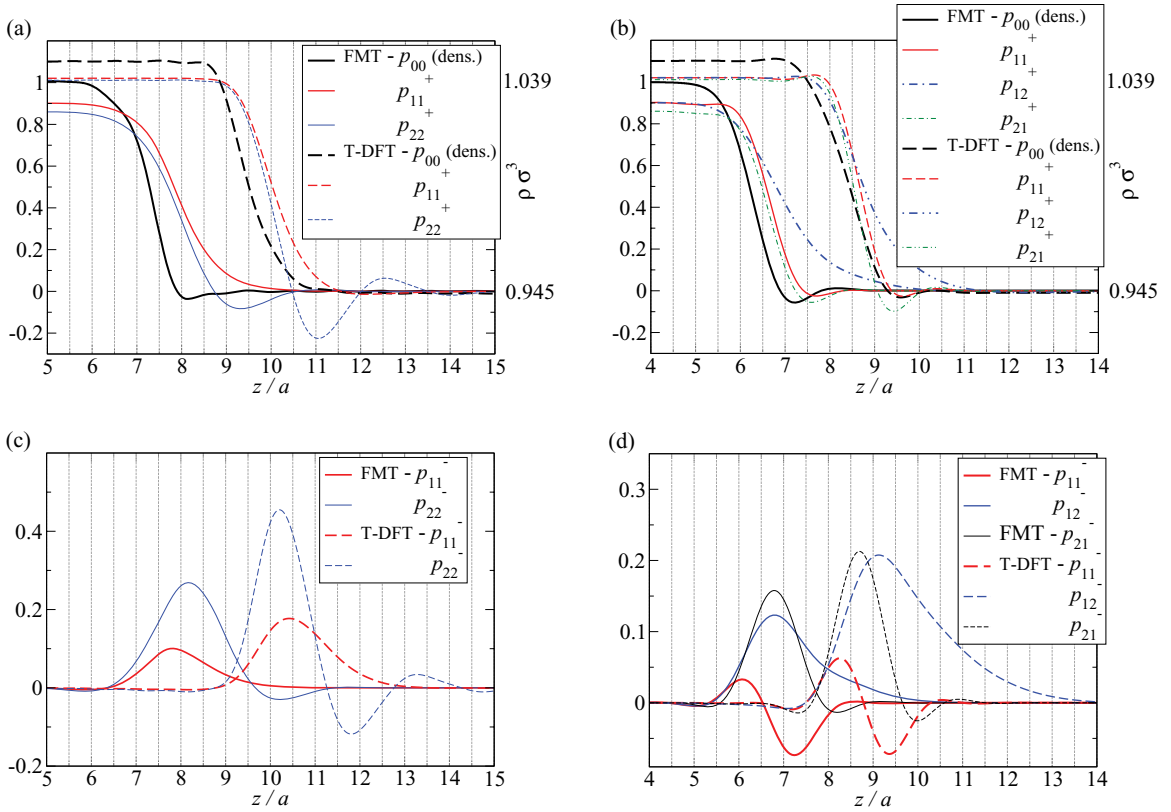

FIG. 6. (Color online) Comparison between mode profiles from FMT and Taylor-expanded DFT (T-DFT, using the PY direct correlation function and $\rho_0\sigma^3 = 0.94$). Note that the interface position for T-DFT is shifted by about $2a$ compared to the interface position for FMT to enhance readability. Real part of leading density modes for (a) the [100] interface and (b) the [111] interface. The density mode $p_{00}(z)$ has been rescaled and shifted; see tick labels at right y axis. Imaginary parts of leading density modes are displayed in (c) for the [100] interface and in (d) for the [111] interface.

each other using the discrete symmetry group of the crystal under consideration. Thus in the bulk crystal, all $p_j(z) \equiv P_j$ associated with these $\mathbf{K}_j$ are equal. For the fcc crystal, the reciprocal lattice is of bcc symmetry. We assume a to be the side length of the cubic unit cell of *fcc* and correspondingly $b = 2\pi/a$ the side length of the cubic unit cell of *bcc* in reciprocal space. The reciprocal basis is given in Cartesian coordinates, where the axes span the cubic unit cell in reciprocal space, by $\mathbf{B}_1 = b(1,1,-1)$, $\mathbf{B}_2 = b(1,-1,1)$, and $\mathbf{B}_3 = b(-1,1,1)$. An arbitrary RLV is a linear combination of the $\mathbf{B}_i$. The shells are characterized by a triple (m,n,k) of natural numbers, and the K_j belonging to this shell have Cartesian components $b(\pm m, \pm n, \pm k)$ and permutations thereof. Thus, if m,n,k are mutually distinct, there is a maximum of 48 RLV in one shell. The shells with lowest modulus are given by (1,1,1), (2,0,0), and (2,2,0). A listing of the RLV triples up to shell 15 is given in Ref. [34] (Table I). At the interface, the degeneracy of the RLV in one shell is lifted, and we introduce an index n which distinguishes the possible values of the z component of the RLV. Thus the decomposition becomes

$$\psi(x,y,z) = \sum_{mn} \sum_{j} p_{mn}(z) \exp[\mathrm{i}(\mathbf{K}_j)_{mn} \cdot \mathbf{r}]. \qquad (41)$$

The sum over j is only for those RLV within shell m which have a common value of z component, as expressed by the index n. In the literature, such a decomposition has been used to parametrize the full 3D density profile using only the leading mode in order to facilitate a simplified order parameter description of the crystal-fluid interface. In the context of PFC, the leading-mode picture has been advanced by Karma *et al.* [35]. If the z component of $(\mathbf{K}_j)_{mn}$ is zero, the mode will be purely real, and if that z component is nonzero, the mode will be in general complex, and we denote by $p^{+}_{mn}(z)$ its real part and by $p^{-}_{mn}(z)$ its imaginary part. The $p^{-}_{mn}(z)$ have the obvious interpretation of *phase shifts* of the associated field oscillations across the interface.

The technique to perform the mode extraction from a full 3D solution $\psi(x,y,z)$ of a system with a solid-liquid interface is described in Ref. [36]. There the density mode properties for the FMT solutions of the hard-sphere interfaces in different orientations have been discussed in detail. Some of these properties can be summarized as follows:

(1) A separation of about one cubic unit cell length $a \approx 1.6\,\sigma$ between the interface location as determined by the average density and the interface location as determined by the leading crystallinity mode $[p_{1n}(z)]$

(2) A small density depletion zone just in front of the bulk crystal [dip in profile $p_{00}(z)$]

(3) Strongly nonmonotonic mode profiles also for next-to-leading modes, especially for $p_{2n}(z)$

(4) Kink position for higher modes $p_{mn}(z)$ shifts towards the bulk crystal for increasing m.

2. *Mode profiles from T-DFT and PFC in comparison with FMT*

First, we compare the leading density modes of the [100] and [111] interfaces for the FMT solutions and the solutions from Taylor-expanded DFT (T-DFT); see Fig. 6. The meaning of the different modes is seen best from the associated RLV. As a basis for the RLV, we choose vectors in direction of the cartesian axes with lengths $2\pi/a_x$, $2\pi/a_y$, and $2\pi/a_z$, respectively. The quantities $a_{x[y,z]}$ are the side lengths of the minimal cuboid fcc unit cells fitting the desired interface orientation in z direction. For a graphical representation, we refer to Ref. [36] (Fig. 2). In Fig. 6 we illustrate the leading mode $p_{11}(z)$ for the [100] orientation (corresponding to $\mathbf{K} = (1,1,1)$, the direction of close-packed planes), and the next-to-leading mode $p_{22}(z)$ [corresponding to $\mathbf{K} = (0,0,2)$, leading oscillation of lateral density average]. For the [111] orientation, the leading mode splits into $p_{11} \leftrightarrow \mathbf{K} = (0,2,1)$ and $p_{12} \leftrightarrow \mathbf{K} = (0,0,3)$. Both RLV correspond to directions of close packed planes, but the mode $p^+_{11}(z)$ clearly differs from $p^+_{12}(z)$. Only the latter has a monotonic shape as expected for a "leading-order" interface profile, similar to $p^+_{11}(z)$ of the [100] orientation. For the next-to-leading mode, we have $p_{21} \leftrightarrow \mathbf{K} = (1,1,2)$. The FMT results for the real parts of these leading modes display already all properties 1–4 listed above. We further remark that the modes from T-DFT compare fairly well on a semiquantitative level. The density depletion zone is missed, and the phase shifts are more pronounced. For both FMT and T-DFT, the mode expansion converges slowly as seen by the plateau values of the modes in the crystalline bulk. This is a consequence of the narrow density peaks in the bulk crystal.

Next we compare the interface mode profiles for the order parameter $\Psi(\mathbf{r})$ from PFC on the one hand and from FMT on the other hand. Here the FMT order parameter follows from the smeared density $\bar{\rho}(\mathbf{r})$ [Eq. (37)], which is rescaled and shifted according to the PFC transformation in Eq. (19). For the PFC parameter, $\epsilon = 0.5$, and a reference density of $\rho_0\sigma^3 = 0.94$, the results for the real part of the leading modes is shown in Fig. 7 [part (a) for the [100] interface and part (b) for the [111] interface]. First, one notes that the absolute magnitude of the PFC modes is smaller by a factor of about 3 compared to the FMT modes. This is a consequence of the different widths of the order parameter peaks in the crystal bulk: They are more narrow in FMT (see Fig. 4), and consequently their Fourier amplitudes are larger. Second, except for the "density" depletion, the mode features identified in FMT are not present in PFC. This is attributed to the simple free energy of the PFC model. Our mode results further illustrate that the specificities of the layered hard-sphere packing cannot be captured by PFC. Another interesting observation is that the interface width w of the [100] interface is about $0.24\,a$ for PFC and $0.86\,a$ for FMT if the leading mode $p_{11}(z)$ is fitted to the simple tanh profile $1 - \tanh[(z - z_0)/w]$. For the [111] orientation we find widths of $0.47\,a$ (PFC) and $1.05\,a$ (FMT) from a fit to the leading mode $p_{12}(z)$. In conclusion, we observe that the width of the interface is much smaller in PFC, and it varies considerably with the orientation of the interface.

3. *Mode profiles from simulations in comparison with FMT*

We have carried out Molecular Dynamics simulations of the [100] interface in order to give a comparison to FMT data as well as to demonstrate the applicability of the mode expansion technique to simulation data. The simulations were carried out in the NVT ensemble at coexistence in cuboid boxes of cross-sectional area of 5 unit cells × 5 unit cells ($L_x \times L_y = 7.84\sigma \times 7.84\sigma$) and a length of $L_z \approx 205\sigma$ with the crystal occupying about 60% of the box volume and placed in the middle of it. We have recorded the laterally averaged density profile

$$\rho_{\mathrm{av}}(z) = \frac{1}{L_x L_y} \int_0^{L_x} dx \int_0^{L_y} dy\, \rho(x,y,z) \tag{42}$$

with a resolution of 64 points per unit cell as a time average over different time intervals T_{av}.

From $\rho_{\mathrm{av}}(z)$ one can extract mode profiles $p_{mn}(z)$ for which the lateral components of the associated reciprocal lattice vector are zero: $(K_x)_{mn} = (K_y)_{mn} = 0$. In particular we focused on the average density mode $p_{00}(z)$ and the first two modes appearing for the lateral density average $p_{22}(z)$ [$(\mathbf{K})_{22} = (0,0,2)$] and $p_{62}(z)$ [$(\mathbf{K})_{62} = (0,0,4)$].

Due to the periodic boundaries of the simulation box, global center of mass motion of the system does not cost any free

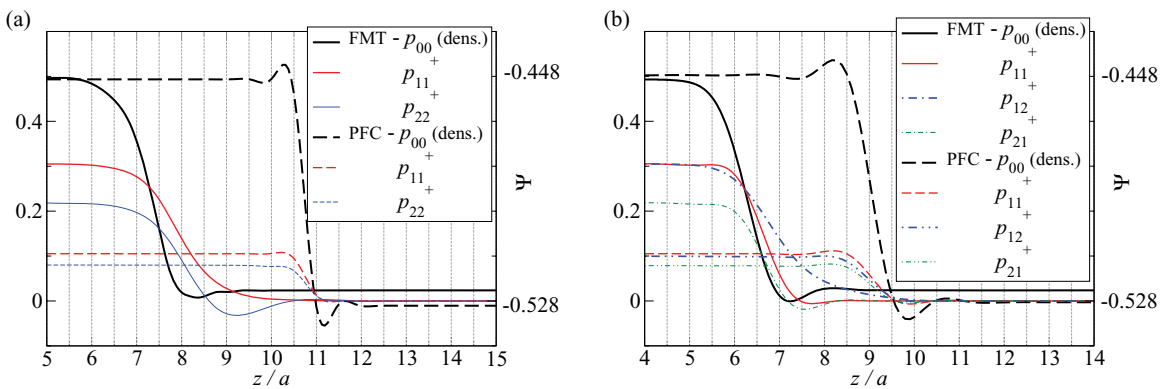

FIG. 7. (Color online) Comparison between order parameter mode profiles from FMT and PFC for the [100] interface in (a) and the [111] interface in (b) for the PFC parameter $\epsilon = 0.5$ (see Fig. 1). The order parameter resulting from FMT is calculated from the 3D FMT density profile by $\Psi(\mathbf{r}) = \sqrt{g/(\rho_0^2 c_4 q_0^4)}\,[\bar{\rho}(\mathbf{r})/\rho_0 - 1 - b/(3g)]$ [see Eqs. (19) and (37), $q_0^2 = c_2/(2c_4)$]. We choose the reference density $\rho_0\sigma^3 = 0.94$. The remaining parameters are given in Table II. To enhance readability the "density" mode $p_{00}(z)$ is rescaled and shifted (see tick labels at right y axis) and that the interface position for PFC is shifted by about $3a$ compared to the interface position for FMT.

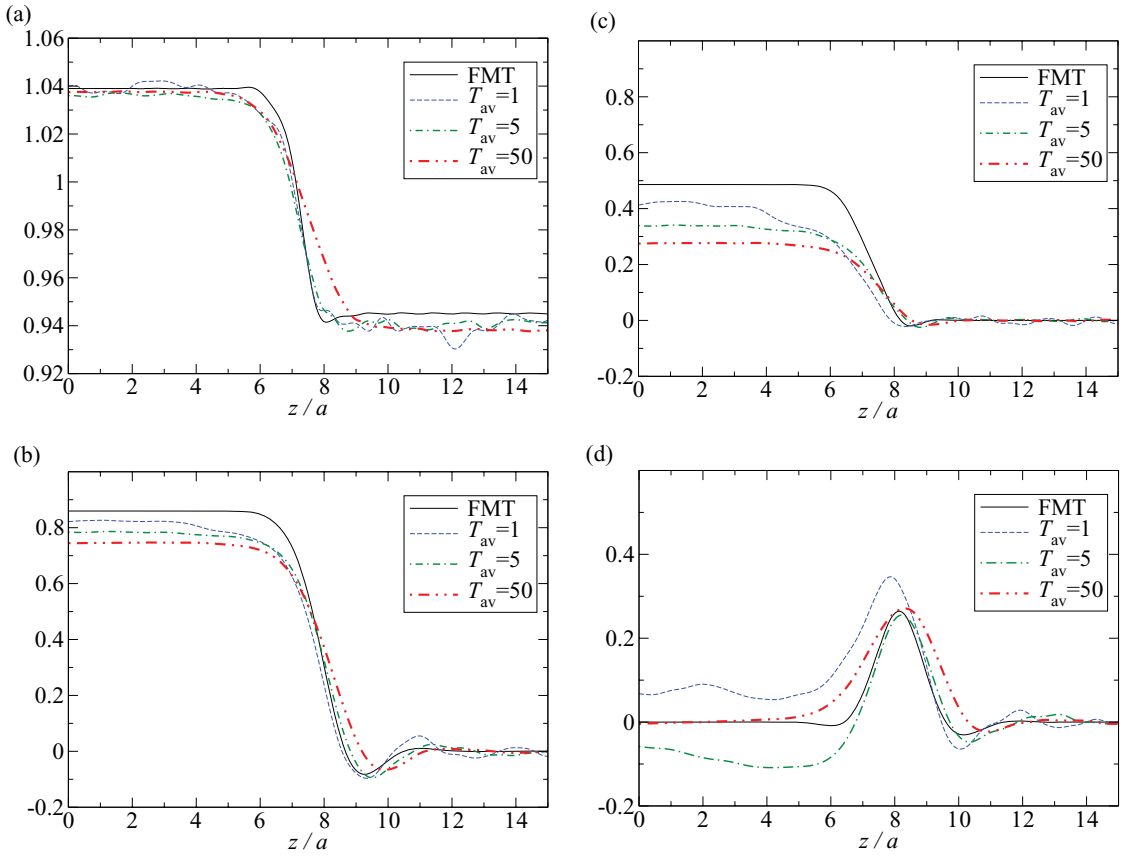

FIG. 8. (Color online) Leading modes extracted from simulated, laterally averaged density profiles in comparison with FMT results. (a) Average density mode $p_{00}(z)$, (b) real part of $p_{22}(z)$ [$(\mathbf{K})_{22} = (0,0,2)$], (c) real part of $p_{62}(z)$ [$(\mathbf{K})_{22} = (0,0,4)$], and (d) imaginary part of $p_{22}(z)$.

energy, hence the system diffuses freely. When taking the time average, we have made no attempt to correct for this motion, as it was negligibly small on the time scale of T_{av}. Furthermore we have not corrected for the zero mode of the capillary waves at the interfaces. The zero mode corresponds to a shift Δz of the average interfacial position, which is caused by fluctuations in the overall amount of crystalline material. For an infinite system, this zero mode would not incur a free energy penalty either. For a finite system adsorption or desorption of crystalline layers results in a density change in the surrounding liquid reservoir. This is associated with a free energy cost, which we estimate in quadratic approximation to be

$$\Delta F = \frac{2L_x L_y}{L_z}(\rho_{\mathrm{cr}} - \rho_{\mathrm{fl}})^2 \mu'_{\mathrm{fl}}(\rho_{\mathrm{fl}})\,(\Delta z)^2\,, \qquad (43)$$

where $\mu'_{\mathrm{fl}}(\rho)$ is the density derivative of the fluid chemical potential. For our system the broadening of the interface due to the zero mode contribution is rather small, $\langle(\Delta z)^2\rangle < 1\ \sigma^2$.

Besides the zero mode, there are also capillary waves with a finite wavelength. It is impossible to disentangle the contribution of capillary interfacial broadening from the width of a hypothetical "intrinsic" density profile which one would like to relate to the profile from density functional theory. However, by studying density averages for different time intervals, we will obtain some qualitative insight regarding the contribution that capillary waves make to the density modes.

In Fig. 8 we show the mode profiles extracted from the simulation data for averaging times of 1, 5, and 50 self-diffusion times τ as well as the FMT counterparts. (We give T_{av} in units of the characteristic self-diffusion time, which it takes a particle in the coexisting liquid to diffuse over a distance of σ.) The width of the average density [Fig. 8(a)] compares well with the FMT profile for $T_{\mathrm{av}} = 1$ and 5 but shows a significant broadening for $T_{\mathrm{av}} = 50$. This we largely ascribe to finite-wavelength capillary waves which are sampled better at longer times. The broadening effect on the mode width is less pronounced for the crystallinity modes [Fig. 8(b)–(d)]. A strong effect of the sampling time is visible on the plateau value in the crystalline part of the real parts of mode p_{22} [Fig. 8(b)] and of mode p_{62} [Fig. 8(c)]. This reflects the broadening of the lattice site density peaks due to diffusion of the crystal as a whole. Apart from that the behavior of the modes in the interface region $z/a = 7, \ldots, 11$ compares very well with the FMT results. In particular the good agreement for the imaginary part of p_{22} signifies that the wavelength shift of the density oscillations across the interface is captured correctly by FMT.

IV. SUMMARY AND CONCLUSION

We have studied the crystal-liquid interface in the hard-sphere system by means of theoretical description on three approximative levels, all of which are based on classical density functional theory (DFT):

(1) Fundamental measure theory (FMT), the currently most accurate theoretical framework for hard spheres

(2) Second-order Taylor-expanded DFT which truncates density fluctuations with respect to a reference density beyond second order

(3) A phase-field crystal (PFC) model which formally can be viewed as local expansion of the second-order Taylor-expanded DFT in density fluctuations and in gradients thereof to fourth order.

Coexistence properties, surface tensions, and interfacial profiles for three interface orientations have been determined in all approximations by free minimization of the associated density functionals. FMT provides us with benchmark results against which the other approximations can be measured. For the [100] interface, we have confirmed that also the interfacial density mode profiles obtained from FMT show good agreement with corresponding results of Molecular Dynamics simulations. Thereby we have demonstrated the applicability of the mode expansion technique to simulation data.

An important difference between FMT on the one hand and Taylor-expanded DFT and PFC on the other hand is that the packing constraints for hard particles are incorporated very well only in the former. In consequence, the small values for the relative vacancy concentration for equilibrium crystals and the relatively small surface tension anisotropy are predicted correctly. Vacancy concentrations in Taylor-expanded DFT and PFC are off by orders of magnitude. The surface tension anisotropy is too large by a factor of two in Taylor-expanded DFT and much too large in PFC. In Taylor-expanded DFT, we find a surprising sensitivity of coexistence properties to details of the direct correlation function. This results in a strong sensitivity of the average surface tension with respect to the choice of the direct correlation function.

We have discussed in detail the problem of parameter fixing in PFC. It turns out that the identification of the PFC order parameter with a rescaled and shifted smeared density is a suitable working recipe. The structure factor and coexistence free energies can be fitted very well. The order parameter distribution in the bulk crystal compares to FMT well only on a qualitative level, but with regard to the surface tension and the interfacial structure there are actually big discrepancies. Our major conclusion here is that the simple PFC variant considered here is too generic and needs to be specifically modified in order to incorporate the hard-sphere like interface structure of fcc materials (see Ref. [37] for an approach in this direction).

The sensitivity of results in Taylor-expanded DFT to the choice of the direct correlation function provides a hint that the specific functional form of the latter should be fitted to obtain proper coexistence. An attempt to match precise results for the direct correlation function (obtained by other means) is perhaps of little practical use. We further discuss that, at least for the hard-sphere system, the status of Taylor-expanded DFT as the reference microscopic DFT for the PFC model is not justified.

The PFC model has become popular also for its computational simplicity when studying dynamic processes such as nucleation and growth. Due to the gradient-expanded form of the free energy, a moderate spatial resolution is needed and larger domains can be studied. Possible numerical solution strategies of the dynamic equation (39) benefit from the experience gained in the study of similar parabolic equations in the literature. However, from our exemplary study here we infer that care is required when one likes to associate the results to particular materials or material classes (such as fcc formers). The basic PFC model (investigated here) can of course be extended (e.g., higher orders in the gradient expansion [11], additional length scales [37]), and these extensions can be used to be more material-specific and hopefully to be more precise in the surface tension and structure, for example. Nevertheless effort is needed for each extension to check and fit the phase diagram and bulk and surface free energies.

In contrast to the easy-to-handle dynamics of the PFC model, apparently no attempt has been reported on the numerical solution of the dynamic DFT equation (11) using FMT functionals for problems involving the solid phase. In view of the performance of FMT with regard to static properties it will be worthwhile to invest some effort in investigating solutions of the dynamic DFT equation. Perhaps it is feasible to combine dynamic DFT and improved PFC models in "mixed resolution schemes," such as has been proposed with the combination of the PFC and the phase-field approach [6].

ACKNOWLEDGMENTS

The authors thank the DFG (German Research Foundation) for support through the Priority Program SPP 1296, grants SCHI 853/2-2, OE 285/1-3, and NE 822/6-3. S.D. acknowledges the National Research Fund, Luxembourg co-funded under the Marie Curie Actions of the European Commission (FP7-COFUND), and the HPC facility of the University of Luxembourg for computing resources.

APPENDIX A: FREE MINIMIZATION OF THE CRYSTAL-FLUID INTERFACE IN DFT

The free minimization of the crystal-fluid interface was achieved by an iterative solution of the Euler-Lagrange equation

$$\rho(\mathbf{r}) = \exp\left[\beta\mu - \frac{\delta(\beta\mathcal{F}^{\mathrm{ex}})}{\delta\rho(\mathbf{r})}\right] = K[\rho], \tag{A1}$$

where the excess free energy $\mathcal{F}^{\mathrm{ex}}$ is given by Eqs. (24) and (26) in the case of FMT and by Eq. (12) in the case of T-DFT, supplemented with the two choices for the direct correlation function [Eq. (30)], given by the coefficients in Eqs. (31) and (32). The density $\rho(\mathbf{r})$ is discretized in a cuboid volume with edge lengths L_x, L_y, and L_z which contains the fluid in the middle ($z \sim L_z/2$) and the crystal phase at the boundaries ($z \sim 0$ and $z \sim L_z$) such that $\rho(x,y,z) = \rho(x,y,L_z - z)$. $L_{x[y]}$ are given by the edge lengths in $x[y]$ direction, $a_{x,[y]}$, of the smallest cuboid unit cell of the crystal which has the desired orientation in the z direction. The crystal cuboid unit cells are shown in Fig. 2 of Ref. [36] for the [100], [110], and [111] orientations. We chose $L_z = 32a_z$ for the [100] and [110] orientations and $L_z = 16a_z$ for the [111] orientation. The equidistant discretization was usually 64 points per unit cell length $a_{x[y][z]}$, but was increased to 128 points per unit cell length $a_{y[z]}$ for the [111] case. All convolution integrals appearing in $\delta\mathcal{F}^{\mathrm{ex}}/\delta\rho$ where calculated using 3D fast Fourier transforms.

As a first step for initialization, bulk crystal density profiles have been determined for the coexisting state. To do so, we determined the minimal free energy per particle of the bulk crystal in the cuboid unit cell at a fixed bulk density ρ_b by solving Eq. (A1) and also minimizing with respect to the unit cell length a (corresponding to a minimization with respect to the vacancy concentration [10]). The coexistence densities ρ_{cr}, ρ_{fl} and the associated chemical potential $\mu = \mu_{coex}$ were determined using the Maxwell construction. The cuboid volume was filled with copies of the bulk crystal unit cell, defining a density profile $\rho_c(\mathbf{r})$. The initial interface profile $\rho_0(\mathbf{r})$ was generated in the following way:

$$\bar{\rho}(z) = \rho_{fl} + (\rho_{cr} - \rho_{fl})\; p(z, z_{0,1}, w_1), \tag{A2}$$

$$\rho_0(x,y,z) = \bar{\rho}(z) + (\rho_c(x,y,z) - \bar{\rho}(z))\; p(z, z_{0,2}, w_2), \tag{A3}$$

$$p(z, z_0, w) = \frac{1}{2}\left(2 - \tanh\left[\frac{z - z_0}{w}\right] - \tanh\left[\frac{L_z - z - z_0}{w}\right]\right). \tag{A4}$$

The advantage of the above prescription is in the separation of the interfacial kink of the average density $\bar{\rho}$ from the kink of the density oscillations through different choices for $z_{0,1}$ and $z_{0,2}$. This is useful to ensure a smooth start into the iterations in the case of FMT; for T-DFT it is not that important.

Iteration was done using a combination of Picard steps with variable mixing and DIIS steps (discrete inversion in iterative subspace) [38]. The Picard steps were performed according to

$$\rho_{i+1}(x,y,z) = \alpha(z)\; K[\rho_i(x,y,z)] + (1 - \alpha(z))\; \rho_i(x,y,z), \tag{A5}$$

$$\alpha(z) = \alpha_{min} + (\alpha_{max} - \alpha_{min}) p'(z, z_0, w), \tag{A6}$$

$$p'(z, z_0, w) = 2 - \tanh^2\left[\frac{z - z_0}{w}\right] - \tanh^2\left[\frac{L_z - z - z_0}{w}\right]. \tag{A7}$$

The mixing function $\alpha(z)$ ensures that there are substantial changes within one iteration step only in the interfacial region, since we chose $\alpha_{min} \sim 10^{-5}$ and $\alpha_{max} \sim 0.001, \ldots, 0.01$. Choosing $\alpha(z) = \text{const.}$ is not practical since the constant would be limited to values below 10^{-4}, otherwise the iteration fails due to instabilities in the bulk crystalline region. The DIIS steps were performed using between $n_{DIIS} = 7, \ldots, 10$ previous profiles.

A typical FMT run consisted of an initial Picard sequence with about 50 steps and $\alpha_{max} = 0.01$. Then we alternated between Picard sequences of a minimum of 10 steps and one DIIS step (which needs another n_{DIIS} Picard initialization steps). We decreased α_{max} after each switch from DIIS to Picard by a factor 1.5 until $\alpha_{max} = 0.001$ was reached. Also, we varied the maximum position of the mixing function $\alpha(z)$ by choosing z_0 randomly in a certain interval (located in the interface region) with a width of about $2\,\sigma$ after each switch from DIIS to Picard. This was done to overcome being trapped at intermediate profiles where the surface tension

$$\gamma = \frac{1}{2a_x a_y}\int_0^{a_x} dx \int_0^{a_y} dy \int_0^{L_z} dz [\beta^{-1}\rho(\mathbf{r})(\ln \rho(\mathbf{r}) - 1] + f^{ex}[\rho(\mathbf{r})] - \mu\rho(\mathbf{r}) + p_{coex}) \tag{A8}$$

hardly changes between iteration steps (f^{ex} is the excess free energy density and p_{coex} is the coexistence pressure). The condition for switching from Picard to DIIS was that after the minimum of 10 steps the convergence parameter

$$\epsilon_i = \frac{1}{a_x a_y L_z}\int_0^{a_x} dx \int_0^{a_y} dy \int_0^{L_z} dz \{K[\rho_i(\mathbf{r})] - \rho_i(\mathbf{r})\}^2 \tag{A9}$$

was decreasing between subsequent steps. If not, the Picard iterations were repeated with another 10 steps until that condition was met. Otherwise DIIS might take one away from the equilibrium solution easily. The DIIS step usually resulted in a very noticeable change in γ and also in ϵ_i in the subsequent Picard steps. It was, however, not possible in general to perform a second DIIS step immediately after the first one since the density profile obtained after this DIIS step lead to singularities in the free energy (local packing fraction $n_3 > 1$). We stopped the run when $\epsilon_i \lesssim 10^{-3}$.

We emphasize that only through the procedure outlined above we were able to determine equilibrium profiles for FMT. The standard method for solving DFT, simple Picard iterations with possibly variable, but spatially constant mixing α, simply fails. Also without DIIS we were not able to arrive at equilibrium profiles within a reasonable time.

For T-DFT, the above procedure does not seem to be necessary but resulted in a very quick convergence.

APPENDIX B: MINIMIZATION OF THE PFC FREE ENERGY FOR THE CRYSTAL-FLUID INTERFACE

In PFC we perform simulations with periodic boundary conditions in each direction, as we do in DFT. In the crystal phase, this implies that a stress will be acting on the crystal unless the dimensions $L_{x[y][z]}$ of the cuboid simulation box fit exactly multiples of the corresponding unit cell lengths of the equilibrium crystal. In order to avoid this stress, we use a simulation box which is minimizing the free energy of the crystal; i.e., we determine the minimizing length of the cubic unit cell $a_{min} := 2\pi/q$ of the fcc crystal (given in dimensionless PFC coordinates, $\mathbf{x} = q_0\mathbf{r}$). For a given average order parameter $\bar{\Psi}_{cr}$, we apply Brent's method to find the box length which minimizes the free energy.

A test for a single crystal cubic unit cell in [100] orientation (for $\epsilon = 0.5$ at coexistence, $\bar{\Psi}_{cr} = -0.448336$) with numbers of points per direction $N = 8$, 16, 32, and 64 has shown that numerical box effects disappear for cubes of edge length 16 and larger. The results for the reciprocal lattice parameters q are $q^{(8)} = 0.539898$, $q^{(16)} = 0.539469$, $q^{(32)} = 0.539476$, and $q^{(64)} = 0.539468$. It is interesting to compare these numbers to the corresponding numbers obtained by expanding the crystal order parameter in reciprocal lattice vectors (see Sec. III D 1) and cutting the expansion at a maximum number n_{sh} for the reciprocal lattice vector shells. We find for $n_{sh} = 4$, 6, 8, and 10 the values $q^{(4)} = 0.53990$, $q^{(6)} = 0.53989$, $q^{(8)} = 0.53956$, and $q^{(10)} = 0.53948$. This demonstrates that n_{sh} corresponds roughly to $N/2$ and that for precise numerical results the few-mode approximation is not quite sufficient.

In order to avoid numerical artifacts, we determine the minimal reciprocal lattice parameters q separately for each orientation; we simulate one unit cell of the crystal with $N = 32$ for the [100] and the [110] interface. The crystal

unit cell in [111] orientation is simulated in a box with discretization $32 \times 64 \times 64$. The cuboid crystal unit cells for the different orientations are the same as used in the DFT calculations (see Fig. 2 of Ref. [36]).

For the initialization of simulations of the crystal-liquid interface, half of the simulation box is filled with a one-mode approximation of the crystal, in [100] orientation given by

$$\Psi(x) = \bar{\Psi}_{\rm cr} + A\cos(qx)\cos(qy)\cos(qz), \qquad \text{(B1)}$$

and the liquid part in the other half has the constant value at coexistence $\bar{\Psi}_{\rm fl}$. The box length in the z direction (perpendicular to the interface) is 32 crystal unit cell lengths for the [100] and [110] orientation, resulting in a simulation box with a total number of points of $32 \times 32 \times 1024$. For the [111] interface, we use 16 unit cell lengths resulting in a box with a total number of points of $32 \times 64 \times 1024$. The crystal resides in one half of the box, so that one interface is in the middle of the box and the other near the periodic boundary.

The PFC simulation evolves according to the dynamic equation (39) until the system relaxes. As an indicator for the relaxation, we use the average deviation $\delta\mu$ of the local chemical potential $\mu(\mathbf{x}) = \delta F_{\rm PFC}/\delta\Psi(\mathbf{x})$ from the coexistence value $\mu_{\rm coex}$ and stopped the computation when $\delta\mu \sim 10^{-4}$.

For the calculation of the dimensionless surface tension $\tilde{\gamma}$ we use the formula

$$2\tilde{\gamma} = \frac{1}{\Omega}\int d^3x \left[f - \left(f_{\rm cr}\frac{\Psi - \bar{\Psi}_{\rm fl}}{\bar{\Psi}_{\rm cr} - \bar{\Psi}_{\rm fl}} - f_{\rm fl}\frac{\Psi - \bar{\Psi}_{\rm cr}}{\bar{\Psi}_{\rm cr} - \bar{\Psi}_{\rm fl}} \right) \right] \qquad \text{(B2)}$$

from Ref. [33], Eq. (50)], where f is the PFC free energy density ($f_{\rm cr}$ for the crystal at coexistence and $f_{\rm fl}$ for the liquid at coexistence). Ψ denotes the PFC order parameter with $\bar{\Psi}_{\rm cr}$ the order parameter average in the coexisting crystal and $\bar{\Psi}_{\rm fl}$ the corresponding average in the coexisting liquid. Ω is the interface area (in dimensionless PFC units). Upon reordering Eq. (B2) we find

$$2\tilde{\gamma} = \frac{1}{\Omega}\int d^3x \left[f + \frac{f_{\rm cr}\bar{\Psi}_{\rm fl} - f_{\rm fl}\bar{\Psi}_{\rm cr}}{\bar{\Psi}_{\rm cr} - \bar{\Psi}_{\rm fl}} - \frac{\Psi}{\bar{\Psi}_{\rm cr} - \bar{\Psi}_{\rm fl}}(f_{\rm cr} - f_{\rm fl}) \right] \qquad \text{(B3)}$$

$$= \frac{1}{\Omega}\left(\int d^3x[f] + \frac{f_{\rm cr}\bar{\Psi}_{\rm fl} - f_{\rm fl}\bar{\Psi}_{\rm cr}}{\bar{\Psi}_{\rm cr} - \bar{\Psi}_{\rm fl}} - \frac{f_{\rm cr} - f_{\rm fl}}{\bar{\Psi}_{\rm cr} - \bar{\Psi}_{\rm fl}}\int d^3x[\Psi] \right) \qquad \text{(B4)}$$

TABLE III. Surface tension $\tilde{\gamma}$ for $\epsilon = 0.53$ in the [100] direction.

N	$\tilde{\gamma}_{[100]}$
8	0.00913
16	0.01041
32	0.01041
64	0.01052

define $\bar{f}$, $\bar{\Psi}$ as volume averages of the free energy density and order parameter

$$= \frac{1}{\Omega}\int d^3x \left[\bar{f} + \frac{f_{\rm cr}\bar{\Psi}_{\rm fl} - f_{\rm fl}\bar{\Psi}_{\rm cr}}{\bar{\Psi}_{\rm cr} - \bar{\Psi}_{\rm fl}} - \frac{f_{\rm cr} - f_{\rm fl}}{\bar{\Psi}_{\rm cr} - \bar{\Psi}_{\rm fl}}\bar{\Psi} \right] \qquad \text{(B5)}$$

$$= \frac{V}{\Omega}\left[\bar{f} + \frac{f_{\rm cr}\bar{\Psi}_{\rm fl} - f_{\rm fl}\bar{\Psi}_{\rm cr}}{\bar{\Psi}_{\rm cr} - \bar{\Psi}_{\rm fl}} - \frac{f_{\rm cr} - f_{\rm fl}}{\bar{\Psi}_{\rm cr} - \bar{\Psi}_{\rm fl}}\bar{\Psi} \right], \qquad \text{(B6)}$$

where $V = \int d^3x = L_x \cdot L_y \cdot L_z$ so $\frac{V}{\Omega} = L_z$, and we obtain

$$\tilde{\gamma} = \frac{L_z}{2}\left[\bar{f} + \frac{f_{\rm cr}\bar{\Psi}_{\rm fl} - f_{\rm fl}\bar{\Psi}_{\rm cr} - \bar{\Psi}(f_{\rm cr} - f_{\rm fl})}{\bar{\Psi}_{\rm cr} - \bar{\Psi}_{\rm fl}} \right]. \qquad \text{(B7)}$$

Note that the factor $\frac{1}{2}$ is needed due to the presence of two interfaces in the simulation.

To calculate the surface tension with Eq. (B7) we calculate $\bar{f}, \bar{\Psi}$ in the whole domain. $\bar{\Psi}_{\rm fl}$, $\bar{\Psi}_{\rm cr}$, $f_{\rm cr}$, and $f_{\rm fl}$ are calculated by convoluting f and Ψ with normalized Gaussians of sufficient width such that the resulting profile is locally constant. This is equivalent to peak to peak averaging of the f and Ψ profiles on the crystal side.

For $\epsilon = 0.53$, results for the surface tension have been reported previously in Ref. [39]. We checked the convergence of the surface tension for different number of points N per unit cell length. For the [100] orientation, the results are given in Table III and should be compared with $\gamma_{[100]} = 0.0113$ from Ref. [39]. For the [111] direction Ref. [39] provides $\gamma_{[111]} = 0.0082$, whereas our result is $\gamma_{[111]} = 0.0079$ (using $N = 32$). It is not clear which precise discretization was used in Ref. [39], but we can conclude that typical discretizations of about 10,...,15 points per unit cell used in the PFC community leave a residual error of about 5% in the value of the surface tension.

[1] H. Emmerich, Adv. Phys. **57**, 1 (2008).
[2] J. J. Hoyt, M. Asta, and A. Karma, Mat. Science Eng. R **41**, 121 (2003).
[3] G. I. Toth and L. Granasy, J. Phys. Chem. B **113**, 5141 (2009).
[4] B. Laird, J. Chem. Phys. **115**, 2887 (2001).
[5] H. Emmerich, H. Löwen, R. Wittkowski, T. Gruhn, G. I. Tóth, G. Tegze, and L. Gránásy, arXiv:1207.0257.
[6] N. Goldenfeld, B. P. Athreya, and J. A. Dantzig, Phys. Rev. E **72**, 020601 (2005).
[7] A. J. Archer and M. Rauscher, J. Phys. A: Math. Gen. **37**, 9325 (2004).
[8] R. Evans, Adv. Phys. **28**, 143 (1979).
[9] T. V. Ramakrishnan and M. Yussouff, Phys. Rev. B **19**, 2775 (1979).
[10] M. Oettel, S. Görig, A. Härtel, H. Löwen, M. Radu, and T. Schilling, Phys. Rev. E **82**, 051404 (2010).
[11] A. Jaatinen, C. V. Achim, K. R. Elder, and T. Ala-Nissila, Phys. Rev. E **80**, 031602 (2009).
[12] P. Hopkins, A. Fortini, A. J. Archer, and M. Schmidt, J. Chem. Phys. **133**, 224505 (2010).
[13] S. L. Singh, A. S. Bharadwaj, and Y. Singh, Phys. Rev. E **83**, 051506 (2011).
[14] K. R. Elder and M. Grant, Phys. Rev. E **70**, 051605 (2004).

[15] S. A. Brazovskii, ZhETF **68**, 175 (1975) [Sov. Phys. JETP **41**, 85 (1975)].
[16] J. Swift and P. C. Hohenberg, Phys. Rev. A **15**, 319 (1977).
[17] G. Gompper and S. Zschocke, Phys. Rev. A **46**, 4836 (1992).
[18] A. Jaatinen and T. Ala–Nissila, J. Phys.: Condens. Matter **22**, 205402 (2010).
[19] Y. Rosenfeld, Phys. Rev. Lett. **63**, 980 (1989).
[20] P. Tarazona, Phys. Rev. Lett. **84**, 694 (2000).
[21] P. Tarazona, J. A. Cuesta, and Y. Martinez-Raton, in *Theory and Simulation of Hard-Sphere Fluids and Related Systems*, edited by A. Mulero, Lecture Notes in Physics 753 (Springer, Berlin, 2008), pp. 247–382.
[22] R. Roth, J. Phys.: Condens. Matter **22**, 063102 (2010).
[23] H. Hansen–Goos and R. Roth, J. Phys.: Condens. Matter **18**, 8413 (2006).
[24] T. Zykova-Timan, J. Horbach, and K. Binder, J. Chem. Phys. **133**, 014705 (2010).
[25] R. L. Davidchack, J. Chem. Phys. **133**, 234701 (2010).
[26] S. K. Kwak, Y. Cahyana, and J. K. Singh, J. Chem. Phys. **128**, 134514 (2008).
[27] A. Härtel, M. Oettel, R. E. Rozas, S. U. Egelhaaf, J. Horbach, and H. Löwen, Phys. Rev. Lett. **108**, 226101 (2012).
[28] L. A. Fernandez, V. Martin-Mayor, B. Seoane, and P. Verrocchio, Phys. Rev. Lett. **108**, 165701 (2012).
[29] M. Oettel, H. Hansen–Goos, P. Bryk, and R. Roth, Europhys. Lett. **85**, 36003 (2009).
[30] V. Botan, F. Pesth, T. Schilling, and M. Oettel, Phys. Rev. E **79**, 061402 (2009).
[31] R. D. Groot, J. P. van der Eerden, and N. M. Faber, J. Chem. Phys. **87**, 2263 (1987).
[32] G. L. Jones and U. Mohanty, Mol. Phys. **54**, 1241 (1985).
[33] K.-A. Wu and A. Karma, Phys. Rev. B **76**, 184107 (2007).
[34] A. D. J. Haymet, J. Chem. Phys. **78**, 4641 (1983).
[35] K. A. Wu, A. Karma, J. J. Hoyt, and M. Asta, Phys. Rev. B **73**, 094101 (2006).
[36] M. Oettel, arXiv:1203.3756 [cond-mat.soft].
[37] K.-A. Wu, A. Adland, and A. Karma, Phys. Rev. E **81**, 061601 (2010).
[38] P. Pulay, Chem. Phys. Lett. **73**, 393 (1980).
[39] S. Tang, R. Backofen, J. Wang, Y. Zhou, A. Voigt, and Y. M. Yu, J. Cryst. Growth **334**, 146 (2011).